Journal of Advanced Ceramics
先进陶瓷
ISSN 2226-4108
CN 10-1154/TQ
清华大学出版社 Tsinghua University Press
SciOpen

J Adv Ceram 2026, **15**: 9221387

https://doi.org/10.26599/JAC.2026.9221387

Research Article

Mechanism-guided large-grain design of Sc–Ce co-doped $BaCoO_3$ dual-phase oxygen electrodes for protonic ceramic cells

Lin Ge*, Xiaole Yu, Xinyuan Zhao, Bingyu He, Maoyi Hua, Yue Luo, Ziru Li,

Jida Wang, Sheng Cui*

College of Materials Science and Engineering, Nanjing Tech University, Nanjing 211816, China

*Corresponding authors:

E-mail: S. Cui, scui@njtech.edu.cn;

L. Ge, gelin2013@njtech.edu.cn

Received: August 12, 2026; Revised: September 16, 2026; Accepted: September 29, 2026

©The Author(s) 2026

Just Accepted

清华大学出版社 Tsinghua University Press | SciOpen

Abstract: Conventional oxygen electrode designs for protonic ceramic cells (PCCs) predominantly rely on the empirical notion that maximizing specific surface area inherently enhances electrochemical performance. However, this paradigm overlooks the critical mismatch between electrode microstructure and the intrinsic rate-determining step (RDS) of the proton-coupled oxygen-reduction-reaction (PC-ORR). In this study, we present a mechanism-driven microstructure engineering strategy that deliberately favors large-particle architectures over nanoscale morphologies to optimize performance when proton transport, rather than surface reaction kinetics, governs the electrode process. By employing Sc-Ce co-doping in $BaCoO_3$, Sc stabilizes the cubic perovskite lattice, while supersaturated Ce induces spontaneous in-situ phase reconstruction, yielding a dual-phase composite electrode composed of ~80 wt.% Co-rich cubic catalytic framework and ~20 wt.% $BaCeO_3$-based nanoscale proton-conducting fillers. Comprehensive electrode reaction pathway analysis reveals that Ce doping shifts the proton migration mechanism from hydration-dehydration to hydrogenation-dehydrogenation, thereby repositioning the RDS to be proton transport-dominated rather than surface-ORR-controlled. Guided by this insight, micrometer-sized particles are employed to establish continuous proton conduction channels. The optimized $BaCo_{0.7}Sc_{0.1}Ce_{0.2}O_{3-\delta}$ electrode demonstrates an ultralow polarization resistance of 0.138 $\Omega \cdot cm^2$ at 600 °C, stable operation exceeding 120 hours, a peak power density of 2.28 $W \cdot cm^{-2}$ in fuel cell mode, and an electrolysis current density of 2.96 $A \cdot cm^{-2}$ at 700 °C, performance metrics that surpass most reported Co-based PCC oxygen electrodes. This work establishes a broadly applicable, mechanism-aligned microstructure design paradigm, challenging the assumption that high surface area is invariably the dominant design parameter. It provides critical guidance for the rational development of advanced protonic ceramic electrochemical devices.

Keywords: protonic ceramic cells, proton coupled oxygen reduction reaction, rate-determining step, in-situ, heterogeneous interfaces

Just Accepted

1 Introduction

Reversible protonic ceramic cells (R-PCCs) represent a promising class of energy conversion devices, notable for their broad fuel flexibility and high Faradaic efficiency.[1-7] Operating efficiently within 400-600 °C, which is enabled by the low activation energy for proton migration, R-PCCs offer a compelling alternative to conventional solid oxide cells that require harsh, high-temperature conditions.[2, 8-12] However, their widespread commercial application remains hindered primarily by the sluggish reaction kinetics of the oxygen electrodes, which must function reliably under humid atmospheres and frequently cycling operation.[13-19] The development of advanced oxygen electrodes entails addressing two intertwined challenges: enhancing electrocatalytic activity for oxygen and evolution reactions (ORR/OER), and ensuring robust structural stability under long-term humid operational conditions.[13, 20-24]

Traditional perovskite oxygen electrodes, especially $BaCoO_3$-based materials, commonly suffer intrinsic structural vulnerabilities such as phase transition-induced microcracking and limited ionic/electronic conduction pathways resulting from sintering.[25, 26] Attempts to improve catalytic activity via single-element doping often exacerbate lattice distortions and cause irreversible structural failure at elevated sintering temperatures.[26] These limitations highlight the urgent need for a rational design strategy that simultaneously balances catalytic performance with structural durability. For decades, oxygen electrode design has predominantly followed a superficial yet pervasive principle: maximizing specific surface to boost catalytic activity[8, 27]. While this holds true for surface-reaction-limited electrodes, this paradigm overlooks a fundamental question—what if the rate-determining step (RDS) is not a surface reaction but bulk ions transport?[28] Most prevailing optimization approaches (such as infiltration,[10, 14] exsolution,[15, 29-31] nano-structuring,[21, 32, 33] and composite formation[34-37]), adhere rigidly to the high-surface-area dogma, without explicitly correlating the electrode microstructure to the intrinsic PC-ORR pathway and RDS.[28] In the case of proton-conducting

Just Accepted

electrodes where bulk proton migration governs performance, excessive nanoscale grain boundaries and interfaces introduced by high-surface-area morphologies can disrupt continuous proton conduction networks, paradoxically impeding overall reaction kinetics. This phenomenon constitutes a critical, yet often overlooked, morphology-mechanism mismatch bottleneck.

Despite extensive effort to advance oxygen electrode materials, very few studies have questioned whether microstructural design should be fundamentally dictated by the intrinsic RDS of the electrode reaction.[28] This oversight has propagated a widespread mismatch: electrodes engineered to maximize surface area inadvertently introduce abundant grain boundaries that block bulk proton transport, the key limiting factor for dehydrogenation-type electrodes.[28] Addressing this gap by rational aligning microstructure with the reaction mechanism is essential for breakthroughs in electrode performance.

Recent studies have identified two distinct PC-ORR pathways that govern oxygen electrode reaction in R-PCC, each defined by a unique RDS[28, 38]. The hydration-dehydration pathway involves a two-step reaction sequence with surface O_2 dissociation as the rate-limiting, surface-controlled step, highly dependent on exposed active sites.[28, 38] Conversely, the hydrogenation-dehydrogenation pathway proceeds via a one-step, proton-coupled reaction dominated by bulk proton migration across the electrode matrix.[28, 38] This mechanistic bifurcation calls for targeted microstructural engineering tailored to specific RDS rather than a universal pursuit of high surface area.

Inspired by the mechanistic understanding of PC-ORR, this work introduces a novel Sc–Ce dual-doping induced in-situ particle gradation strategy to develop high-performance oxygen electrodes. Sc doping stabilizes the cubic perovskite framework of $BaCo_{0.9}Sc_{0.1}O_3$ (BCS), suppressing polymorphic phase transition and eliminating sintering-derived microcracks.[25, 26] Beyond the solid solubility limit, Ce doping induces spontaneous in-situ phase reconstruction, resulting in a dual-phase composite electrode comprising a Co-rich catalytic phase (C-BCSCe2) forming a continuous framework and nano-sized $BaCeO_3$-based proton-conducting phase (P-BCO) serving as fillers within $BaCo_{0.7}Sc_{0.1}Ce_{0.2}O_{3-\delta}$ (BCSCe2).[14, 39] Ce and Sc modulate the electron structure and B-site ion

Just Accepted

coordination, shifting the PC-ORR mechanism from hydration-dehydration in BCS to hydrogenation-dehydrogenation in BCSCe2.[28]

Critically, guided by a comprehensive mechanistic understanding of the RDS, this study strategically aligns electrode microstructure with the underlying reaction kinetics. Specifically, the dehydrogenation-type BCSCe2 oxygen electrode, where bulk proton transport is rate-limiting, employs large particles to form uninterrupted proton conduction pathways, while in-situ precipitated P-BCO nanoparticles reinforce interfacial adhesion and substantially increase the density of active reaction sites. This deliberate microstructural design culminates in a BCSCe2 oxygen electrode exhibiting ultralow polarization resistance alongside remarkable long-term cycling stability. Consequently, R-PCCs incorporating the BCSCe2 oxygen electrode achieve a peak power density of 2.28 W cm^{-2} in fuel cell mode and a current density of 2.96 A cm^{-2} at 1.3 V during electrolysis at 700 °C, manifesting its strong potential as a highly efficient bifunctional oxygen electrode for intermediate-temperature R-PCCs. Beyond demonstrating that high surface area is not invariably the dominant design criterion for this dual-phase electrode, this work establishes a broadly applicable, mechanism-guided microstructure engineering framework to rationally develop advanced protonic ceramic oxygen electrodes.

2 Experimental and Calculation Methods

2.1 Materials preparation

A series of perovskite-type electrode powders, including $BaCoO_3$, $BaCo_{0.9}Sc_{0.1}O_3$ and $BaCo_{0.9-x}Sc_{0.1}Ce_xO_3$ (BCSCe*x*, *x*=0.1, 0.2, 0.3) electrode powders were synthesized via a citrate-ethylenediaminetetraacetic acid (EDTA) complexing sol-gel route. Stoichiometric amounts of $Ba(NO_3)_2$, $Sc(NO_3)_3 \cdot 4H_2O$, $Co(NO_3)_2 \cdot 6H_2O$ and $Ce(NO_3)_3 \cdot 6H_2O$ were first fully dissolved in deionized water under magnetic stirring. Citric acid and EDTA were then added as dual chelating agents to guarantee uniform complexation of all metal cations, and the pH of the mixed solution was

Just Accepted

adjusted to approximately 8 by dropwise addition of aqueous ammonia. The resulting solution was heated to around 90 °C with continuous agitation to evaporate excess water until a viscous wet gel formed. The gel product was transferred to a drying oven and held for 5 h to obtain a dry xerogel precursor. The solid precursor was cooled to room temperature and ground using a mortar and pestle. After an intense combustion process in a muffle furnace, the ash obtained was calcined at 1000 °C for 5 h. The $BaZr_{0.1}Ce_{0.7}Y_{0.1}Yb_{0.1}O_{3-\delta}$ electrolyte (BZCYYb) powder was prepared following the same sol-gel procedure described above. Commercial NiO powder purchased from Aladdin Reagent was used directly as the anode raw material.

For comparative study, the M-BCSCe2 sample was fabricated through a conventional solid-state reaction method using $BaCO_3$, Co_3O_4, Sc_2O_3 and CeO_2. The weighed oxide and carbonate powders were mixed by planetary ball milling at 300 rpm for 24 h, dried in an oven, and then calcined at 1000 °C for 5 h.

2.2 Materials characterization:

The phase composition and crystal structure of the as-prepared powder samples were characterized by X-ray diffraction (XRD, ARL-X'TRA) using Cu Kα radiation (λ = 1.5406 Å) over a 2θ scanning range of 20°-80°. Qualitative phase identification was performed to confirm the formation of the target perovskite phase, and quantitative phase analysis was further conducted to determine the relative content of each crystalline phase.

The microstructural features of the fabricated cells were observed via scanning electron microscopy (SEM, JEOL, Japan). SEM characterization was mainly applied to: (i) examine the particle size distribution of the cathode powders, (ii) analyze the cross-sectional morphology of the single cells, and (iii) evaluate the interfacial contact between the electrode and electrolyte. Energy-dispersive X-ray spectroscopy (EDS) coupled with the SEM system was used for qualitative and semi-quantitative analysis of elemental composition and spatial distribution on the electrode surface.

Just Accepted

X-ray photoelectron spectroscopy (XPS, K-Alpha, Thermo Fisher Scientific, USA) was employed to investigate the surface chemical states of the electrode materials. All collected spectra were calibrated using the C 1s reference peak at 284.8 eV, and peak deconvolution was carried out with Avantage software to determine elemental valence states, relative atomic concentrations and the dis tribution of different oxygen species. The testing instrument for the thermogravimetric curve is Beijing Hengjiu Experimental Equipment Co., Ltd HQT-4. The X-ray absorption spectroscopy (XAS) measurements were conducted using easyXAFS-300+. TOF-SIMS were conducted by TOF-SIMS IONTOF M6 instrument (IONTOF GmbH) after 24 h hydration in 3%H_2O at 600 °C. BET surface area measurements were conducted via nitrogen adsorption–desorption isotherms recorded at 77 K using a Quantachrome and Micromeritics ASAP 2460 gas sorption analyzer.

For thermal expansion measurements and total conductivity measurements, BCSC*ex* air electrode powders were uniaxially pressed into bar-shaped specimens (3 × 3 × 25 mm^3) followed by sintering at 1100 °C for 5 h to achieve dense ceramics. The thermal expansion coefficients (TECs) were determined using a push-rod dilatometer (NETZSCH DIL 402PC) under air atmosphere, with temperature ramping from 40 °C to 800 °C at a constant heating rate of 5 °C/min. The conductivities of the samples were tested at temperatures ranging from 400 to 800 °C under dry air using the direct current four-probe technique. The electrical conductivity (σ) was calculated according to the Eq(1).

$$\sigma = \frac{L}{A} \times \frac{dI}{dV} \tag{1}$$

Electrochemical impedance spectroscopy (EIS) measurements were performed on a CHI 660e electrochemical workstation (Shanghai Chenhua Instrument Co., Ltd.) over a frequency range of 0.01 Hz to 100 kHz. Distribution of relaxation times (DRT) analysis was implemented using a MATLAB-based DRT toolbox to deconvolute the impedance spectra and distinguish the individual electrochemical reaction processes. Single-cell discharge performance was evaluated at 600–700 °C with humidified H_2 (3 vol% H_2O) supplied as the fuel gas, during which current–voltage (I–V) curves and corresponding impedance spectra were collected simultaneously. All cells were hermetically

Just Accepted

mounted on the test fixture using a high-temperature ceramic sealant (SA-6700, Nanjing Tech University) to ensure gas tightness throughout the electrochemical tests.

The proton conduction in the M-BCSCe2 and N-BCSCe2 samples was evaluated using an optimized Hebb-Wagner direct current polarization method. BZCYYb electrolyte layers were employed as blocking electrodes in symmetric BZCYYb|BCSCe2|BZCYYb pellet cells to isolate protonic transport over the temperature range of 200-500 °C under extremely low pO_2 (~10^{-25} atm) conductions. Under these conditions, electron and oxide-ion conduction are fully suppressed, ensuring that protons constitute the sole charge carrier across the BCSCe2 layer. [10] A constant current (galvanostatic mode) was applied in the range of 1×10^{-3} to 1×10^{-6} A, and the resulting steady-state voltage, time-independent and stable, was recorded. The effective proton conductivity of the BCSCe2 sample was then determined using Eq. (2), after subtracting the ohmic resistance contributions from both BZCYYb blocking electrodes.[10]

$$\sigma_{electrode(proton)} = \frac{1}{\frac{U_{measured}}{I} - \frac{L_{BZCYYb-1}}{\sigma_{BZCYYb} \times S} - \frac{L_{BZCYYb-2}}{\sigma_{BZCYYb} \times S}} \cdot \frac{L_{electrode}}{S} \quad (2)$$

Where $L_{BZCYYb-1}$, $L_{BZCYYb-2}$, and $L_{electrode}$ represent the thicknesses of the upper blocking layer, lower blocking layer, and the mixed-conducting samples, respectively. S denotes the electrochemically active area of the measurement system, I is the applied constant current, and $U_{measured}$ is the measured steady-state voltage. The bulk conductivity of BZCYYb blocking layers (σ_{BZCYYb}) was independently determined via Eq. (3), using impedance spectra acquired under identical low oxygen partial pressures (~10^{-25} atm).

$$\sigma_{BZCYYb} = \frac{L}{R_{ohmic} \times S} \quad (3)$$

2.3 Fabrication and characterization of the symmetric and single cells

Just Accepted

Anode-supported single cells featuring a three-layer configuration (comprising a porous anode support, dense electrolyte film, and porous cathode) were fabricated in this work. The NiO-BZCYYb anode support was prepared via a conventional solid-state reaction route. Briefly, BZCYYb powder, NiO, and starch pore former were mixed at a mass ratio of 6:4:1 and homogenized through mechanical ball milling to form the anode precursor powder. A co-pressing technique was employed to assemble the half-cell green body: initially, 0.3 g of anode powder was uniaxially pre-pressed to form the supporting substrate; subsequently, 0.02 g of BZCYYb electrolyte powder was evenly spread atop the preformed anode layer, followed by co-pressing under increased pressure to ensure intimate interfacial contact. The resultant green half-cell was sintered at 1450 °C for 5 h in a high-temperature furnace, yielding a dense BZCYYb electrolyte film firmly bonded to the porous NiO-BZCYYb anode support. The electrode paste was prepared by mixing electrode powder with a binder solution of ethyl cellulose and terpineol in a mass ratio of 1:1.2. This paste was then applied onto the electrolyte surface via screen printing and subsequently sintered at 950 °C for 2 hours to form the porous electrode layer.

2.4 Computational methods:

All density functional theory (DFT) calculations were conducted using the CASTEP (Cambridge Serial Total Energy Package) code, employing OFTG ultrasoft pseudopotentials and a spin-polarized framework for all simulations.[40] The Perdew–Burke–Ernzerhof (PBE) functional within the generalized gradient approximation (GGA) was utilized to describe electron exchange–correlation interactions. To account for the strong on-site Coulomb interactions of Co *3d* and Ce *4f* electrons, the PBE+U scheme was applied with U values of 3.3 eV for Co and 5.0 eV for Ce. A plane-wave cutoff energy of 500 eV was used, and the magnetic moment of Co was fixed at 1.8 μ_B. Structural models were constructed as 2×2×2 supercells of the BCSCe perovskite lattice. Geometry optimizations were deemed converged when the total energy change fell below 1×10^{-5} eV and the maximum Hellmann–Feynman force on each atom was under 0.03 eV/Å. Electronic structure calculations, including band

Just Accepted

structure and density of states analyses, were performed using a k-point mesh corresponding to a grid spacing of 0.025 $Å^{-1}$. Proton migration was modeled within the same 2×2×2 supercell. Work-function and heterointerface simulations employed slab models cleaved along the (001) plane with a vacuum layer thickness of 15 Å. The oxygen p-band center (ε_p) was calculated using the following expression:

$$\varepsilon_p = \frac{\int_{-\infty}^{\infty} n_p(\varepsilon)\varepsilon d\varepsilon}{\int_{-\infty}^{\infty} n_p(\varepsilon) d\varepsilon} \quad (4)$$

The oxygen vacancy formation energy (E_{Vo}) was calculated as:

$$E_{Vo} = E_{defect} - E_{perfect} - \frac{1}{2}E_{O_2} \quad (5)$$

where E_{defect} denotes the energy of the perovskite with an oxygen vacancy, E_{O2} is the energy of O_2.

The hydration energy (E_{hydra}) was calculated as:[41]

$$E_{hydra} = E_{2OH} - E_{defect} - E_{H_2O} \quad (6)$$

where E_{2OH} is the energy of the crystal with two additional protons, E_{defect} is the energy of the defective bulk and E_{H2O} is the energy of an H_2O molecule.

3 Results and Discussion

3.1 Phase Characterization

In $BaCoO_3$ perovskites, the active Jahn-Teller (J-T) distortion of Co^{3+} ions combined with a high tolerance factor (t≈1.09) stabilizes the material in a hexagonal crystal structure (space group P63/mmc).[35] Introducing Sc^{3+} ions, which have a larger ionic radius (~0.745Å) compared to Co^{3+} (~0.61Å) and Co^{4+} (~0.53Å), modifies the tolerance factor from 1.09 to approximately 0.97.[26] The rigid ScO_6 octahedron suppress the J-T distortion induced by CoO_6 octahedron, thereby promoting a phase transition from the original hexagonal structure (P63/mmc) to a cubic perovskite phase (Pm3m).[25, 26] X-ray diffractions (XRD) analyses (Figure 1a) confirm that 10 mol% Sc-doping transforms $BaCoO_3$ ($BaCo_{0.9}Sc_{0.1}O_3$, BCS) from hexagonal to cubic symmetry, consistent with

Just Accepted

previous reports by Lee et al.[26] This structural transition leads to higher lattice symmetry, which is known to facilitate faster ionic and electronic transport within the crystal lattice, thus potentially enhancing ORR/OER.

Building upon this foundation, we systematically investigated the effect of increasing Ce doping on the phase structure of Ce-substituted BCS-based samples: $BaCo_{0.8}Sc_{0.1}Ce_{0.1}O_{3-\delta}$ (BCSCe1), $BaCo_{0.7}Sc_{0.1}Ce_{0.2}O_{3-\delta}$ (BCSCe2), and $BaCo_{0.6}Sc_{0.1}Ce_{0.3}O_{3-\delta}$ (BCSCe3). As shown in Figures 1a-b and S1, increasing Ce content induces the progressive emergence and growth of a secondary $BaCeO_3$ phase. Simultaneously, the diffraction peaks of the primary $BaCoO_3$ phase systematically shift toward lower angles, indicating lattice expansion. This behavior is attributed to the larger ionic radii of Ce^{3+}/Ce^{4+} (r=1.01 Å / 0.87 Å) compared to Co^{2+}/Co^{3+} (r=0.745 Å / 0.61 Å), confirming successful Ce incorporation into the BCS lattice up to a critical solubility threshold. Rietveld refinement (Figure 1c, S1 and Table S1) provide quantitative analysis of phase composition and lattice parameters across the doping series. BCSCe1 mainly consists of the cubic perovskite C-BCSCe phase (a=b=c= 4.1153 Å), with a minor fraction of the proton-conductive $BaCeO_3$ (P-BCO) phase (a=b=c= 4.3443 Å). For BCSCe2, the dominant cubic phase (79.9 wt.%) exhibits lattice expansion to a=b=c=4.1318 Å, while the P-BCO phase correspondingly increases to 20.1wt.%(a=b=c=4.4004 Å). At higher Ce content (BCSCe3), the lattice parameter of the main phase (70.2 wt.%) plateaus at a=b=c= 4.1334 Å, whereas the P-BCO phase fraction rises sharply to 29.8 wt.%. This disproportionate increase in the secondary phase beyond 20 mol% Ce doping indicates that the solubility limit in the cubic BCS lattice has been reached, with excess Ce ions precipitating as $BaCeO_3$ rather than substituting into the lattice.

Further structural insights into BCS and BCSCe2 powders were obtained via high-resolution transmission electron microscopy (HR-TEM) combined with strain mapping. Figure 1d reveals lattice fringes with a 0.282 nm, corresponding to the (110) planes of the cubic $BaCoO_3$ phase (Pm3m), confirming lattice stabilization attributable to Sc doping.[25, 26] In BCSCe2 (Figure 1e), lattice fringes of 0.136 nm and 0.195 nm are assigned to the (221) planes of C-BCSCe and the (210) planes of P-

Just Accepted

BCO, respectively, evidencing the coexistence of these distinct phases formed via in-situ phase reconstruction.

To understand the interfacial strain induced by the lattice mismatch between C-BCSCe and P-BCO phases, geometric phase analysis (GPA) was performed on HR-TEM images (Figure 1f).[42] The strain maps display heterogeneous distributions of normal strains (ε_{xx}, ε_{yy}) and shear strain (ε_{xy}), with alternating tensile and compressive regions reflecting local lattice distortions. This tensile strain within the P-BCO phase likely arises from lattice mismatch and has been reported to enhance charge carrier mobility and catalytic in electrode materials.[42]

Energy-dispersive X-ray spectroscopy (EDS) coupled with TEM (Figure 1g) confirms the uniform nanoscale particle morphology and elemental distribution within BCSCe2. Ce is homogeneously distributed alongside Ba, Sc, and O, attesting to successful lattice doping without local segregation. In contrast, Co exhibits localized enrichment corresponding to the C-BCSCe phase domains. Point EDS analysis (Figure S2) further distinguishes these phases: point A(Co ~53.15 wt%, Ce ~6.88 wt%) matches C-BCSCe, whereas point B (Co ~5.13 wt%, Ce ~53.81%) corresponds to P-BCO. These results corroborate the Ce-induced in-situ dual-phase formation in BCS perovskites. The formation of proton-conductive P-BCO phase is expected to enhance proton transport within the electrode, thereby improving its electrochemical performance for PCC applications.

Just Accepted

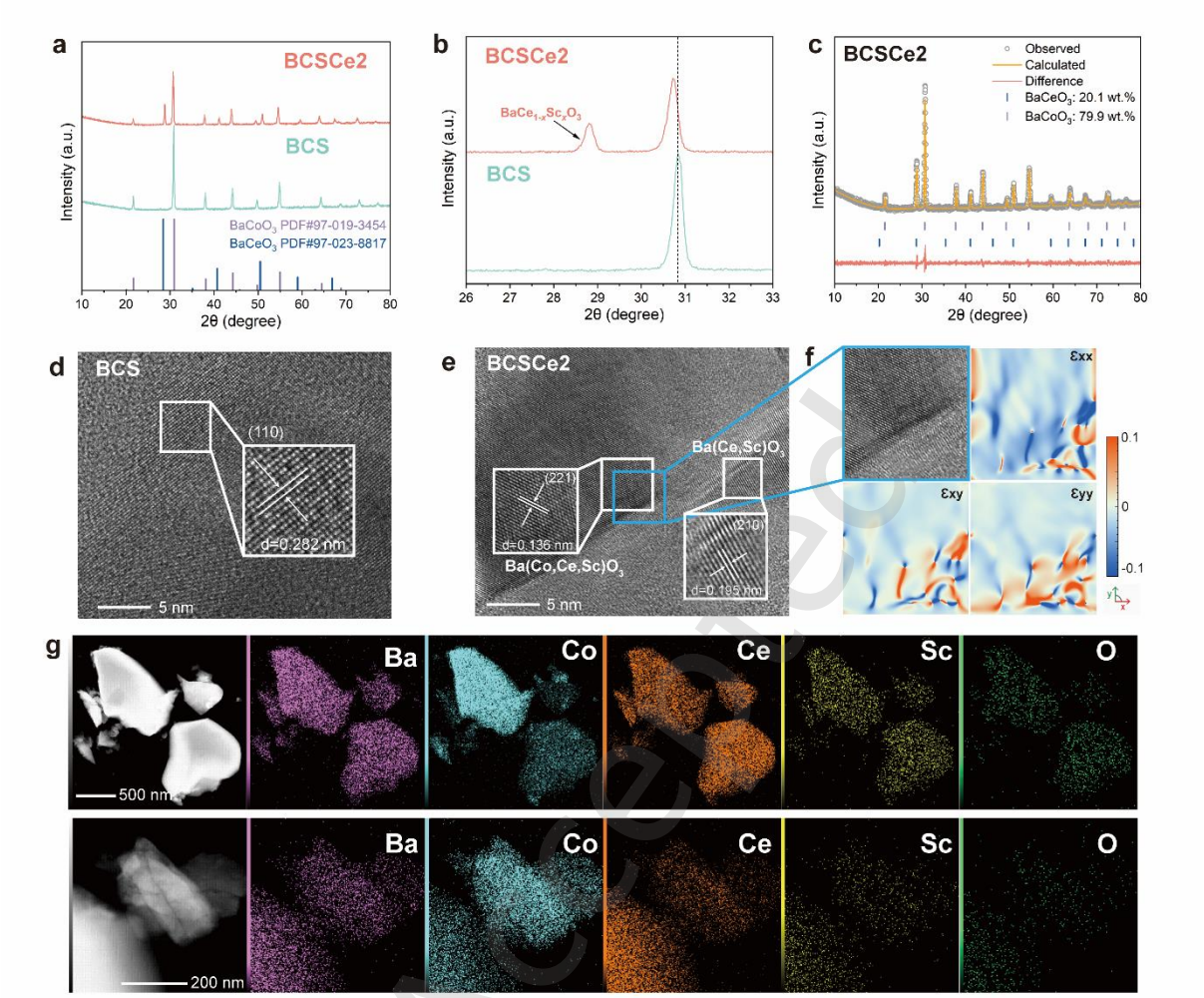


Figure 1. (a) and (b) XRD patterns of the BCSCe2 and BCS series oxides, along with PDF cards showing different phases. (c) Refined XRD profiles of the BCSCe2 sample. (d) and (e) TEM images of BCS and BCSCe2 sample. (f) The GPA analysis of BCSCe2 sample. (g) The EDS mapping results of BCSCe2 samples.

3.2 Electrochemical performance

With increasing content of the proton-conductive P-BCO phase, the electrochemical performance and proton transport properties of Ce-doped BCS samples are expected to improve. To systematically assess this, BCS, BCSCe1, BCSCe2, and BCSCe3 electrodes were comprehensively evaluated. In this section, Ce-doped BCS sample are synthesized at 1000 °C for 5h by sol-gel method and calcined at 950 °C for 2h to prepared symmetrical cells. Symmetrical cells with configuration Ag | BCSCe2 | BZCYYb | BCSCe2 | Ag were fabricated to probe ORR and OER activities. As shown in Figure 2a and b, electrochemical impedance spectroscopy (EIS) measurements were conducted in an air

Just Accepted

atmosphere containing 3% H_2O within the temperature range of 600–700°C. Notably, BCSCe2 exhibited the lowest area-specific resistance (ASR) values of 0.06, 0.13, and 0.37 $\Omega \cdot cm^2$ at 700, 650, and 600°C , respectively—significantly outperforming BCS, BCSCe1, and BCSCe3, which showed ASRs of 0.76, 0.46, and 0.91 $\Omega \cdot cm^2$ at 600°C, respectively (Figures 2b, S3-S4). These results highlight that optimal Ce doping and formation of the C-BCSCe/P-BCO heterointerface markedly enhance electrode kinetics, likely by facilitating improved proton transport and accelerating oxygen diffusion and exchange.

Further insight into the reaction kinetics was gained by constructing Arrhenius plots of the natural logarithm of polarization resistance (lnRp) against reciprocal of temperature (1000/T) (Figure 2c). All samples display linear behavior, indicative of thermally activated processes dominated by oxygen surface exchange and charge transfer. Calculated activation energies (E_a) are 136.93, 82.80, 139.70, and 171.51 $kJ \cdot mol^{-1}$ for BCS, BCSCe1, BCSCe2, and BCSCe3, respectively. The intermediate E_a and lowest ASR of BCSCe2 suggest an optimal balance between reaction kinetics and structural stability conferred by its composition and microstructure.[43, 44]

To elucidate individual electrochemical processes, the distributed relaxation time (DRT) analysis was conducted on EIS data (Figure 2d). The resulting DRT spectra can be deconvoluted into three distinct frequency regimes: high-frequency (HF, >10 kHz), intermediate-frequency (IF, 10 Hz–10 kHz), and low-frequency (LF, 0.01–10 Hz).[10, 43, 45] The BCSCe2 sample shows a notably enhanced HF response, which corresponds to charge-transfer processes at the triple-phase boundaries (TPB), indicative of improved charge-transfer kinetics across the electrode/electrolyte interface and within the electrode bulk. [43] The IF region is associated with surface oxygen exchange and bulk diffusion dynamics, while the LF processes are predominantly governed by gas diffusion of oxygen and water vapor to the active sites.[31] Among all samples studied, BCSCe2 exhibits the lowest IF and LF resistances, indicating superior oxygen species transport and enhanced gas diffusion kinetics.

Just Accepted

The total electrical conductivity, representing combined electronic and oxide-ion conduction (e^- + O^{2-}), is critical for electrode performance at intermediate temperatures. Conductivity measurements from 350 and 800 °C (Figure 2e) indicate typical p-type semiconducting behavior in both BCS and BCSCe2, with monotonic increases in conductivity upon heating.[25, 31, 43] BCS consistently exhibits higher conductivity than BCSCe2, reaching ~4.0 S·cm^{-1} at 800 °C versus ~1.4 S·cm^{-1} in BCSCe2. The difference arises primarily from higher hole carrier concentration and uninterrupted Co^{4+}–O^{2-}–Co^{3+} electronic pathways in BCS. In contrast, Sc substitution and multi-element doping in BCSCe2 dilute the Co^{4+}/Co^{3+} redox hopping network and introduce electron scattering centers, leading to reduced conductivity. These findings align with prior reports on Sc-doped barium cobaltate perovskite systems.[31, 46]

To corroborate the enhanced oxygen surface exchange and proton transport properties fo BCSCe2, electronic conductivity relaxation (ECR) experiments were conducted under stepwise variations in oxygen and water vapor partial pressures (Figure S5).[39] Upon switching oxygen partial pressure from 0 to 0.21 atm, the relaxation times for BCSCe2 and BCS were measured to be 255 s and 400 s, respectively, confirming significantly accelerated oxygen exchange dynamics in BCSCe2. Consistently, the derived chemical surface exchange rates (k_{chem}) and chemical diffusion coefficients of oxygen ($D_{O,\,chem}$) further substantiate this improvement: BCSCe2 exhibits $D_{O,\,chem}$ =3.98 × 10^{-3} cm s^{-1} and k_{chem} =8.655 × 10^{-4} cm^2 s^{-1}, markedly surpassing those of BCS ($D_{O,\,chem}$ = 2.12 × 10^{-3} cm s^{-1}, k_{chem} = 2.648 × 10^{-4} cm^2 s^{-1}).

Thermal expansion coefficient (TEC) compatibility between electrodes and electrolytes is critical to preventing mechanical failure during thermal cycling.[36, 37] Figure 2f illustrates the normalized linear thermal expansion profiles of BCS and BCSCe2 from room temperature to 800°C. BCS exhibits a TEC of 14.91×10^{-6} K^{-1}, whereas BCSCe2 shows a more favorable and closer match to typical electrolytes (~13×10^{-6} K^{-1}) [30, 36, 37] with a TEC of 12.10×10^{-6} K^{-1}. This improved compatibility is

Just Accepted

expected to enhance the structural integrity and mechanical stability of the electrode/electrolyte interface.

The durability of the BCSCe2|BZCYYb|Ag half-cell was evaluated at -1 A cm^{-2} and 600 °C for 120 hours. Two distinct degradation regimes were observed in the voltage profile: an initial relatively rapid voltage decay rate of 1.46 mV h^{-1} during the first 20 hours, corresponding to the cell stabilization process, followed by a markedly suppressed degradation rate of 0.105 mV h^{-1} over the subsequent 100 hours. This overall stability compares favorably with many reported proton-conducting oxygen electrodes. Furthermore, cycling durability tests alternating between fuel cell and electrolysis modes over 60 hours, with current switching between ±1A cm^{-2} every 10 hours, showing moderate degradation (Figure S7). In FC mode, the voltage degradation rates were 0.795 mV h^{-1} and 0.69 mV h^{-1} for the first and second cycles, respectively, with the slightly reduced decay in the latter cycle suggesting a mitigation of degradation kinetics after the initial stage. In EC mode, an initially high voltage degradation rate of 3.11 mV h^{-1} was shown in Figure S7, which significantly decreased to 0.515 mV h^{-1} in the subsequent cycle, indicating substantially suppressed irreversible degradation. Although the initial degradation rate remains relatively high, this declining trend demonstrates that the BCSCe2 electrode holds considerable promise for improved stability upon further optimization.[21, 47, 48]

Single-cell performance of BCSCe2 was evaluated in an anode-supported configuration (BCSCe2 | BZCYYb | Ni-BZCYYb) with a 10 μm thick electrolyte (Figure 2h). Peak power density of 1.73, 1.26 and 0.76 W cm^{-2} were attained at 700, 650 and 600 °C, respectively, while electrolysis current densities reached 2.81, 1.64 and 0.98 A cm^{-2} at 1.3 V, (Figure 2i, S8). In comparison, BCS electrode yielded lower peak densities of 1.16, 0.9 and 0.62 W cm^{-2} and current densities of 1.97, 1.33 and 0.8 A cm^{-2} at corresponding temperatures (Figure 2j, S9). The BCSCe2 demonstrated significantly reduced polarization resistance (0.23, 0.12 and 0.04 Ω cm^{-2} at 600, 650 and 700 °C, respectively), outperforming BCS electrodes. Relative to other Ce-doped samples (BCSCe1 and BCSCe3), BCSCe2

Just Accepted

revealed enhancements of approximately 35.1%—48.6% in electrochemical activity (Figures S10-S11), underscoring the efficacy of Ce doping and in-situ P-BCO phase formation in facilitating enhanced proton conduction and overall electrode performance.

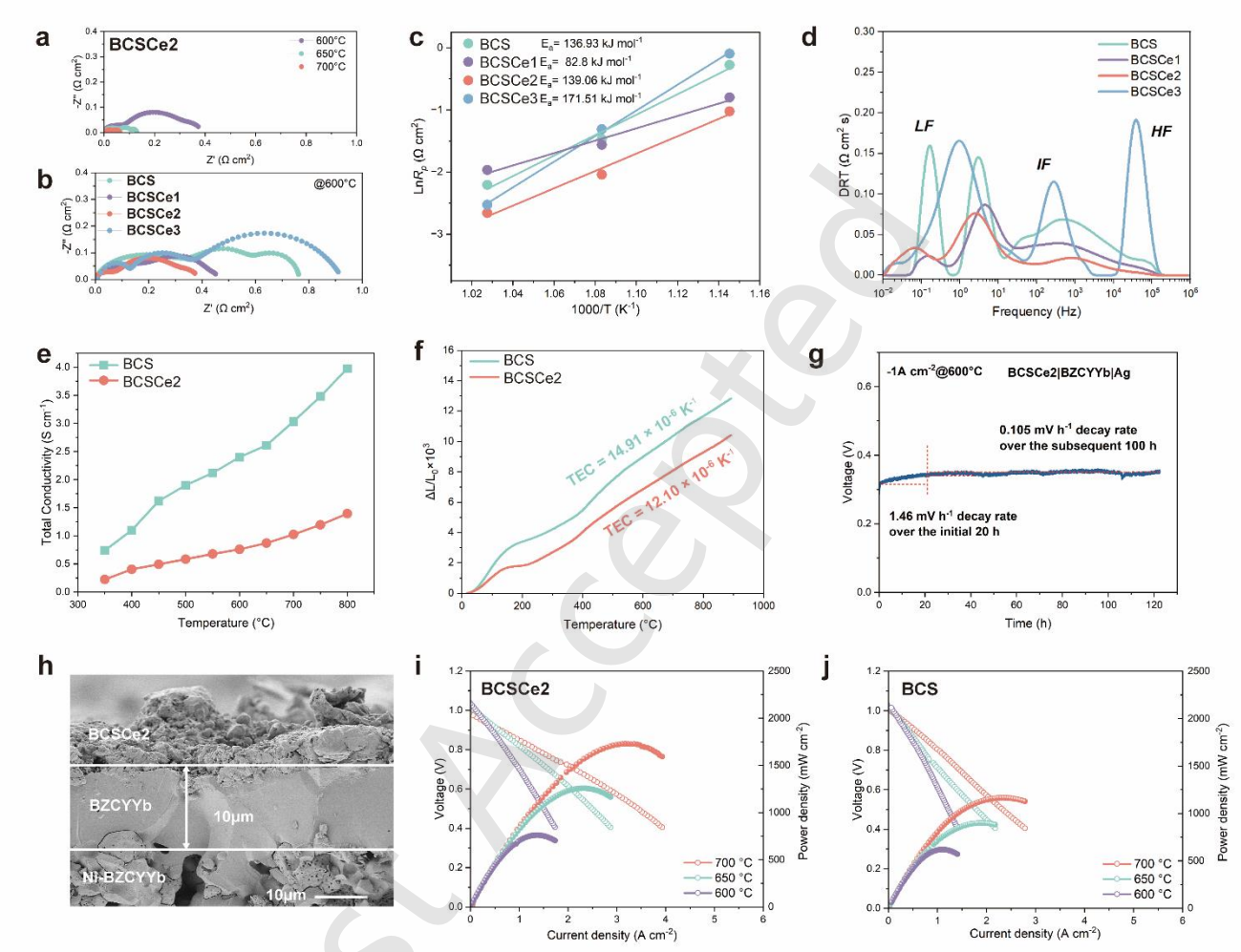


Figure 2. (a–b) EIS spectra of BCSCe2 and the BCS-based perovskite series materials. (c) Arrhenius plots of R_p of series materials. (d) The DRT curves of BCS-based perovskite series materials at 600 °C. (e) Total conductivity of BCS and BCSCe2 samples in air from 350 to 800 °C. (f) The TEC curves of BCSCe2 and BCS from 0 to 800 °C. (g) Durability test of BCSCe2 |BZCYYb| Ag half-cell for 120 h. (h) cross-section SEM images of single cell with BCSCe2 oxygen electrode. I-V-P plots of (i) BCSCe2 oxygen electrode and (j) BCS oxygen electrode.

3.3 Characterizations and calculations of Ce doping in BCS oxygen electrode

In oxygen electrodes, the transition metal elements occupying the B-site play a central role in determining the ORR and OER activities. Doping at B-site profoundly modifies the surface electronic

Just Accepted

structure and oxygen species distribution within perovskite frameworks, thereby critically influencing their catalytic performance.[26, 39, 43, 46] To elucidate the effects of Sc and Ce co-doping on the valence states and oxygen species in BCS and BCSCe2, X-ray photoelectron spectroscopy (XPS) analyses were conducted. Figure 3a and Table S2 present the Co *2p* spectra for BCS and BCSCe2. Both samples exhibit typical Co *2p* spin-orbit splitting peaks ($2p_{1/2}$ and $2p_{3/2}$).[25, 26] The peaks near ~779.8 eV and ~795 eV correspond to the Ba *3d* doublet. Deconvolution of the Co $2p_{3/2}$ and Co $2p_{1/2}$ spectra reveals two pairs of sub-peaks attributed to Co^{3+} and Co^{4+} oxidation states: the lower binding energy peaks (~777.8 eV and ~793.2 eV) are assigned to Co^{3+}, while the higher binding energy peaks (~782.0 eV and ~796.4 eV) correspond to Co^{4+}. Compared to pristine BCS, BCSCe2 exhibits a substantial increase in the Co^{3+} peak area fraction, from 64.9% to 85.8%, concomitant with a decrease in average Co valence from 3.35 (BCS) to 3.14 (BCSCe2). This shift arises from charge compensation induced by Ce doping, Ce^{4+} substitution reduces the oxidation state of Co to maintain overall charge neutrality. The elevated Co^{3+} content indicates a higher population of Co atoms in high-spin states, featuring more unpaired electrons in the e_g orbitals, which is favorable for accelerating ORR and OER kinetics. Moreover, high-spin Co^{3+} may elongate Co-O bonds within CoO_6 octahedron, facilitating the oxygen vacancies formation.[25, 26]

To probe differences in Co electronic configuration and local coordination structure between BCS and BCSCe2, Co K-edge X-ray absorption fine structure (XAFS) characterization including X-ray absorption near edge structure (XANES), Fourier-transform extended X-ray absorption fine structure (EXAFS) and wavelet transform (WT) EXAFS were performed (Figure 3b-e).[25] Normalized Co K-edge XANES spectra (Figure 3b) show that the absorption edge correlates positively with the average oxidation state of Co. The edge of BCSCe2 shifts toward lower energy relative to BCS, corroborating XPS findings of reduced Co valence upon Ce doping.[49] The pre-edge peak near 7709 eV, arising from dipole-forbidden *1s→3d* transitions sensitive to CoO_6 octahedral symmetry, is attenuated in BCSCe2, indicating enhanced Jahn–Teller distortion and symmetry breaking. Such structural perturbations

Just Accepted

disrupt electron pathway, explaining the decreased electronic conductivity observed experimentally in BCSCe2. The inset of Figure 3b magnifies the near-edge region from 7720 to 7724 eV, vividly confirming the negative shift in absorption edge due to Ce^{4+} charge compensation.[25, 49]

Fitted Fourier-transformed EXAFS |χ(R)| curves of Co K-edge (Figure 3c and Figure S12) further elucidate local coordination changes.[25] The prominent peak at ~1.6–1.8 Å corresponds to first-shell Co–O coordination, while weaker peaks at greater distance arise from second-shell Co–Sc/Co–Ba scattering.[25] Compared to BCS, the Co–O peak in BCSCe2 shifts to larger radial distance with diminished intensity, evidencing bond elongation and increased structural disorder in the oxygen coordination environment. The elongation weakens Co–O bonds, lowering oxygen vacancy formation energy and promoting oxygen ion mobility, consistent with XPS results. Concurrently, reduction second-shell peak intensity implies heightened lattice disorder and local strain due to Ce co-doping.[43, 49]

WT-EXAFS contour maps (Figures 3d, 3e) resolve overlapping scattering signals in *k*-*R* space, discriminating atomic coordination paths.[25, 49] The intense lobes at low *R* (~1.6–2.0 Å) and $k \approx 4$–8 $Å^{-1}$ correspond to first-shell Co–O scattering, whereas features at *R* = 2.5–3.5 Å indicate second-shell Co–Sc/Co–Ce inter-cation. BCS exhibits stronger, more localized Co–O WT intensity, reflecting a more ordered Co–O environment.[25] Upon Ce co-doping (BCSCe2), Co–O lobes broaden in both *k* and *R* directions with decreased peak magnitude, signaling increased fluctuations of Co–O bond length and elevated coordination disorder. Notably, a distinct Co–Ce scattering feature emerges in the second shell of BCSCe2, absent in solely Sc-doped BCS, directly confirming successful Ce substitution at B-sites and formation of Co–Ce proximate coordination. This Ce-induced local disorder modulates the Co e_g orbital occupancy and facilitates oxygen vacancy generation, thereby enhancing electrocatalytic kinetics of ORR and OER.[25, 47]

Density functional theory (DFT) calculations using Ba8Co7Sc1O24 (BCS) and Ba8Co6Sc1Ce1O24 (BCSCe) models further elucidate the impact of Ce doping on electron structure

Just Accepted

(Figure 3f). Spin-resolved projected density of states (PDOS) analysis reveals that Ce incorporation shifts the Co *d*-band center upward from -5.08 eV to -4.96 eV and the O *p*-band center from -3.12 eV to -2.99 eV, effectively bringing both Co *3d* and O *2p* orbitals closer to the Fermi level.[35, 39, 44] This concurrent upward shift facilitates the formation of oxygen vacancies and optimizes the adsorption of oxygen intermediates, thereby synergistically improving ORR/OER catalytic activity. [43] Moreover, the elevation in the Co *d*-band center indicates an increased fraction of high-spin Co^{3+} species in BCSCe.

O *1s* XPS spectra (Figure 3g and Table S3) identify four distinct oxygen species: lattice oxygen (O^{2-}, ~528.5 eV), peroxide/hole-related oxygen species (O_2^{2-}/O^-, ~529.0 eV), hydroxyl oxygen (OH^- /O_2, ~531.3 eV), and adsorbed H_2O/CO_3^{2-} (~532.8 eV).[35, 43] [29]Quantitative deconvolution reveals a higher relative concentrations of chemisorbed oxygen species in BCSCe2 compared to BCS. The ratio of chemisorbed oxygen (O_{ads}) to lattice oxygen (O_{lat}), a proxy for oxygen vacancy concentration, increases from 4.45 in BCS to 6.25 in BCSCe2, substantiating enhanced oxygen vacancy generation consistent with the Co valence state analysis.

Thermogravimetric analysis under dry and humid atmospheres (Figure 3h) further confirms these findings. At 800°C under wet conditions, BCSCe2 exhibits a mass loss of 1.33%, approximately double that of BCS (0.65%). Under dry conditions, BCSCe2 also shows a larger mass loss (0.71%) compared to BCS (0.19%).[25, 35, 43] Mass loss in dry air atmosphere corresponds to oxygen vacancy content, while mass change in humid atmosphere reflects hydration behavior. Higher oxygen vacancy concentrations promote lattice oxygen activation favorable for oxygen adsorption and ionic conductivity. Simultaneously, hydration measurements suggest that Ce doping enhances water adsorption and incorporation under humid conditions, improving proton conductivity while mitigating competitive adsorption of H_2O/CO_2 on active sites, thereby enhancing structural stability and electrochemical performance.

Just Accepted

DFT-calculated formation energies of oxygen vacancies and hydration energies at Ce-O-Co sites (Figure 3i) reveal that BCSCe exhibits slightly lower oxygen vacancies formation energy (0.6 eV vs. 0.65 eV) and more exothermic hydration energy (-1.85 eV vs. -1.3 eV) compared to BCS , consistent with experimental XPS and TGA data and indicating increased vacancy and proton incorporation potential.[24, 43] Additionally, proton migration barriers computed along octahedral networks (Figure S13) show reduced barriers in BCSCe (0.73 eV) versus BCS (0.85 eV), verifying that Ce doping facilitates proton transport, aligning with observed enhanced hydration capacity and proton diffusion rates.[25, 35] In summary, Ce doping in the BCS lattice effectively modulates the electron structure by lowering the average valence of Co and weakening Co-O bonds via charge compensation. These changes shift both Co *d*-band and O *p*-band center upwards, reduce the oxygen vacancies formation energy and hydration energy at Ce-related sites, and synergistically enhance oxygen vacancy concentration, proton conductivity, and electrocatalytic activity, ultimately improving the ORR/OER performance of the BCSCe2 oxygen electrode.

Besides, the P-BCO/C-BCSCe heterointerface plays a crucial role in the electrocatalytic performance of the oxygen electrode. To gain deeper insight into the interfacial effect, work functions (WF) and difference charge density calculations were conducted on slab models and the P-BCO (001) / C- BCSCe (001) heterostructure.[50] The Figure S14 displays the electrostatic potential profiles along the surface normal enabled the quantitative evaluation of WF values for three representative phases, which follow the order: BCS (5.461 eV) > BCSCe (5.302 eV) > P-BCO (4.011 eV). The lowered WF of BCSCe relative to pristine BCS indicates an upward-shifted Fermi level and a reduced electron escape barrier, enhancing surface charge transfer capability and favoring oxygen intermediate adsorption thermodynamically.[50] Notably, the substantial WF difference of 1.291 eV between the catalytic C- BCSCe phase and proton-conducting P-BCO phase drives spontaneous interfacial charge redistribution at the in-situ formed heterointerface. Electrons transfer from the low-WF P-BCO to the high-WF BCSCe until equilibration of their Fermi levels, establishing a built-in electric field at the

Just Accepted

phase boundary.[47, 50] This interfacial electric field is expected to accelerate proton and charge transport, expand the electrochemically active triple-phase boundary, and strengthen interphase bonding, thereby providing a key electronic mechanism underpinning the enhanced reaction kinetics and operational stability of the dual-phase oxygen electrode.

Differential charge density calculations of the C- BCSCe (001) / P-BCO (001) heterostructure model (Figure S15)[30, 47, 50] reveal significant electronic interactions at the heterointerface (Z ≈ 9–11 Å), characterized by pronounced charge depletion localized in P-BCO and concurrent charge accumulation in C- BCSCe. These findings confirm the formation of chemical bonding rather than mere physical contact between the two phases. The calculated potential difference across the BCSCe/P-BCO heterointerface reaches 2.986 eV, which facilitates proton and charge transport, reduces interfacial resistance, and effectively extends the triple-phase boundary region.[35, 51] The synergy between the continuous proton conduction channels in P-BCO and abundant high-spin Co^{3+} active sites in C- BCSCe cooperatively accelerates ORR/OER kinetics, comprehensively explaining the superior electrochemical performance observed for the BCSCe2 electrode. In conclusion, Ce doping combined with the in-situ formation of the C-BCSCe/P-BCO heterointerface substantially modulates the electronic structure, promotes proton migration, and optimizes interface charge distribution, collectively contributing to the remarkable enhancement in both electrochemical activity and stability of the BCSCe2 oxygen electrode in PCCs.

The above-discussed electronic structure modulations (including weakened Co-O bonds, increased oxygen vacancies concentration, reduced work function, and enhanced proton migration) collectively imply a fundamental alteration in the oxygen reduction mechanism. Specifically, the enhanced bulk proton mobility coupled with reduced surface rection barrier suggests a transition in the RDS from surface reaction control to bulk transport control upon Ce doping. This hypothesis will be rigorously evaluated in the subsequent section through systematic PC-ORR pathway analysis.

Just Accepted

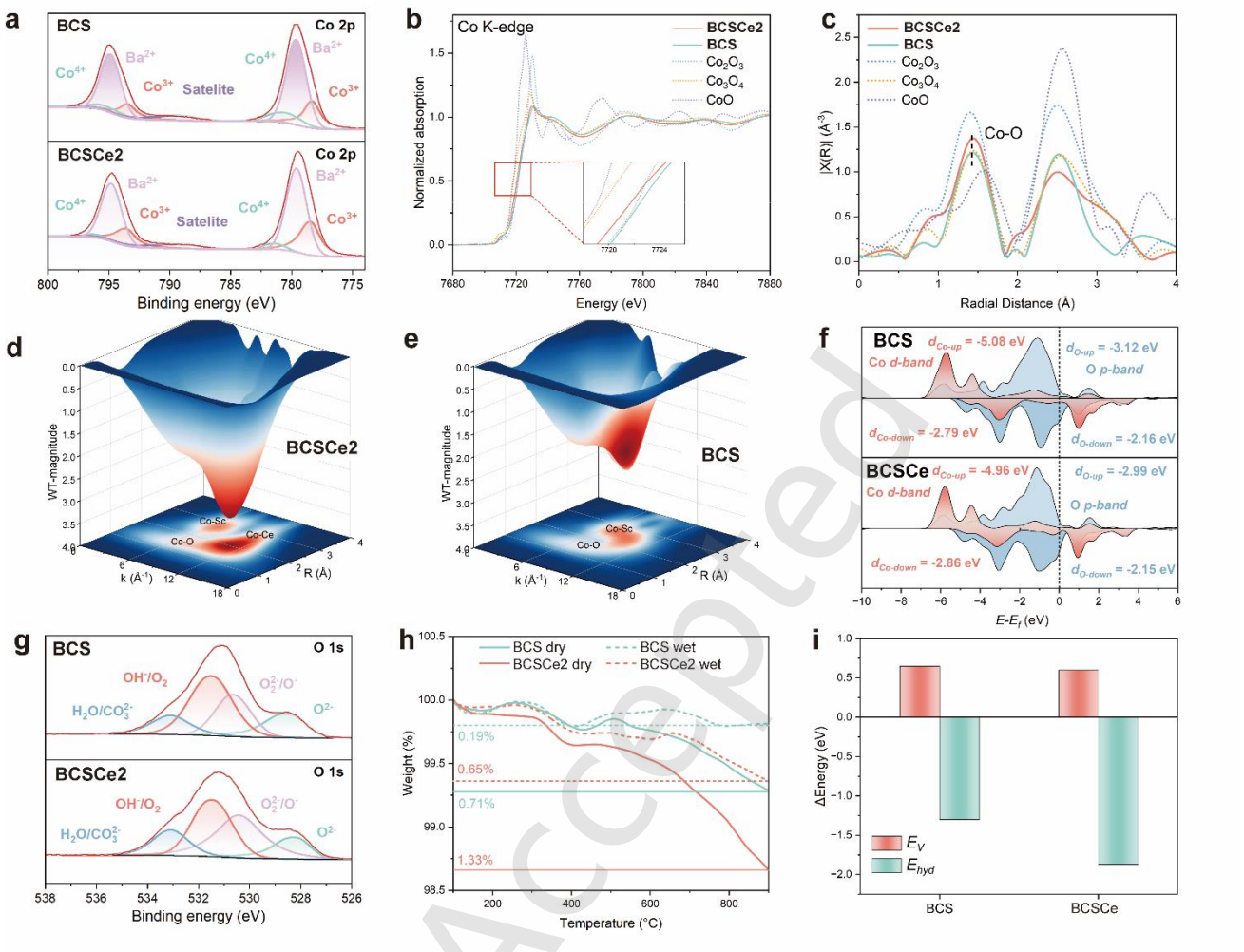


Figure 3. (a) XPS spectra of Co 2p for BCS and BCSCe2 samples. (b) Co K-edge XANES spectra, (c) Fourier-transformed EXAFS spectra (|χ(R)|) of BCS and BCSCe2, with CoO, Co_3O_4 and Co_2O_3 as reference standards. Wavelet-transform EXAFS contour plot of (d) BCSCe2 and (e) BCS samples. (f) The PDOS of BCS and BCSCe sample (g) XPS spectra of O 1s for BCS and BCSCe2 samples. (h) Thermogravimetric analysis (TGA) curves of BCS and BCSCe2 under dry and wet atmospheres. (i) The oxygen vacancies formation energy and hydration energy of BCS and BCSCe samples.

Just Accepted

3.4 Analysis of proton-coupled ORR pathway of BCS and BCSCe2 oxygen electrode

Recently, Ji et al. proposed a new PC-ORR framework that classifies traditional oxygen electrodes into two distinct PC-ORR mechanisms: the hydrogenation mechanism and the hydration mechanism.[28, 38] As schematically illustrated in Figure 4a, the hydrogenation (dehydrogenation) pathway proceeds via a one-step PC-ORR process wherein proton incorporation consumes electronic

holes, thereby reducing the bulk hole concentration and causing a measurable decrease in total electrical conductivity under elevated water partial pressure.[28] In contrast, the dehydration mechanism (Figure 4b) involves a sequential two-step process comprising the traditional ORR followed by a dehydration reaction.[16, 28] Here, charge neutrality is maintained by mutual compensation between protons and oxygen vacancies without altering the hole concentration, resulting in negligible conductivity changes upon variation of water vapor partial pressure. Since the reaction predominantly occurs at oxygen vacancies near the surface rather than involving direct proton participation at surface sites, the RDS remains the surface oxygen exchange reaction.[16] These two PC-ORR mechanisms can be experimentally distinguished by measuring ECR response to step changes in water partial pressure. Electrodes following the hydrogenation mechanism exhibit pronounced conductivity variation and relaxation dynamics in response to vapor pressure changes, whereas electrodes adhering to hydration mechanism demonstrate negligible conductivity response. In order to fully exploit the performance potential of the Ce-doped BCS synthesized herein and provide a design guideline grounded in mechanistic understanding, a systematic investigation of the rate-limiting steps was performed combining ECR, EIS and DRT analysis.

For BCSCe2 (Figure 4c and Figure S16), ECR measurements were conducted by switching the water vapor partial pressure from 0 to 0.03 atm at 600 °C. The raw electrical conductivity data (Figure S16) exhibit a decrease following the increase in vapor partial pressure. The normalized ECR signal (Figure 4c) shows a well-defined, time-dependent relaxation toward a new steady state within approximately 600 s. This pronounced relaxation behavior directly confirms that proton incorporation consumes electronic holes, consistent with a hydrogenation/dehydrogenation charge compensation mechanism.[36, 52] The well-resolved relaxation curve allows for quantitative extraction of proton-related kinetic parameters, including the surface exchange coefficient k_{chem} and chemical diffusion coefficient D_{chem}. These results validate that both dominant bulk proton transport and surface exchange proceed via a one-step hydrogenation pathway in the BCSCe2 electrode.[28, 51]

Just Accepted

In contrast, the BCS (Figure 4d) exhibits negligible conductivity change (~2.33 S cm^{-1}) under identical humidity switching, showing only minor fluctuations without any discernible relaxation. This pH_2O-independent conductivity indicates that the hole carrier concentration remains essentially unchanged by proton uptake, a definitive signature of the hydration/dehydration mechanism. In this case, protons and oxygen vacancies mutually compensate charges without affecting the hole population, thus precluding reliable extraction of proton-related kinetic parameters from ECR analysis (Figure S6). Accordingly, the cathodic process in BCS proceeds via a two-step mechanism involving conventional oxygen reduction coupled with surface dehydration, with oxygen vacancies serving as the critical active sites.[28] Notably, the shift in proton uptake mechanism observed in BCSCe2 can be contributed to two coexisting factors: (i) Ce doping enhances hydration and proton incorporation capabilities, thereby improving the kinetics of interfacial proton transport; (ii) the formation of a P-BCO secondary phase further expands bulk proton conduction pathways and broadens the PC-ORR active region based on percolation theory.

Furthermore, the involvement of protons in the electrode reaction is further substantiated by EIS and DRT analyses under varying water vapor partial pressure (from 0.03 atm to 0.4 atm). [28] Figure 4e (BCSCe2) reveals that increasing pH_2O from 3% to 40% induces a significant and continuous decrease in the total polarization resistance. This pronounced pH_2O sensitivity confirms the direct participation of protons in the electrode reaction, consistent with a one-step hydrogenation mechanism involving proton-coupled surface reactions.[28, 35] In contrast, Figure 4g (BCS) shows minimal variation in impedance arc across the pH_2O range, indicating that the RDS is proton-independent. This behavior aligns with the oxygen vacancy-assisted dissociation of O_2, characteristic of the conventional two-step dehydration ORR. The DRT spectra (Figure 4f, h-j) deconvolve the total polarization resistance into three relaxation processes: high-frequency (HF), intermediate-frequency (IF), and low-frequency (LF) peaks, generally assigned to interfacial ion transport, bulk species diffusion, and surface reaction kinetics, respectively.[10, 43] As shown in Figure 4i and j, the relationship between

Just Accepted

log(ASR) and log(pH_2O) reveals that BCS sample exhibits minimal dependence on water vapor concentration, whereas the BCSCe2 sample shows a strong dependence (n=0.13±0.02), particularly in the LF region, which is closely related to water-involved surface reactions and gas-phase water diffusion. [28, 35, 36, 53]

In summary, BCS operates primarily via a hydration-dehydration mechanism, with the main electrochemical reaction sites located at the electrode/electrolyte interface and hydration sites rather than the electrode surface.[28] Consequently, oxygen must be dissociated into oxygen ions and be transported through the BCS phase toward the bulk to participate in electrode reactions. In this scenario, the oxygen reduction reaction rate becomes the RDS. Conversely, BCSCe2 functions via a hydrogenation-dehydrogenation mechanism. Under this hydrogenation mechanism, protons migrate more readily through the bulk phase compared to the hydration mechanism, allowing protons to transport from the bulk to the surface and react with oxygen ions.[28] In this case, the RDS depends on both proton diffusion rate and ORR kinetics. As shown in Figure 4k, if the bulk proton diffusion coefficient ($D_{chem,proton}$) exceeds the surface oxygen exchange coefficient ($k_{chem,O}$), the surface ORR reaction is the RDS. If the $D_{chem,proton}$ is lower than $k_{chem,O}$, bulk proton diffusion limits the rate. For BCSCe2, $D_{chem,proton} = 6.681\times 10^{-4}$ cm s^{-1} is slightly lower than $k_{chem,O} = 8.655 \times 10^{-4}$ cm^2 s^{-1}, suggesting that improving bulk proton diffusion could further enhance the electrochemical performance of the BCSCe2 oxygen electrode.[28]

Just Accepted

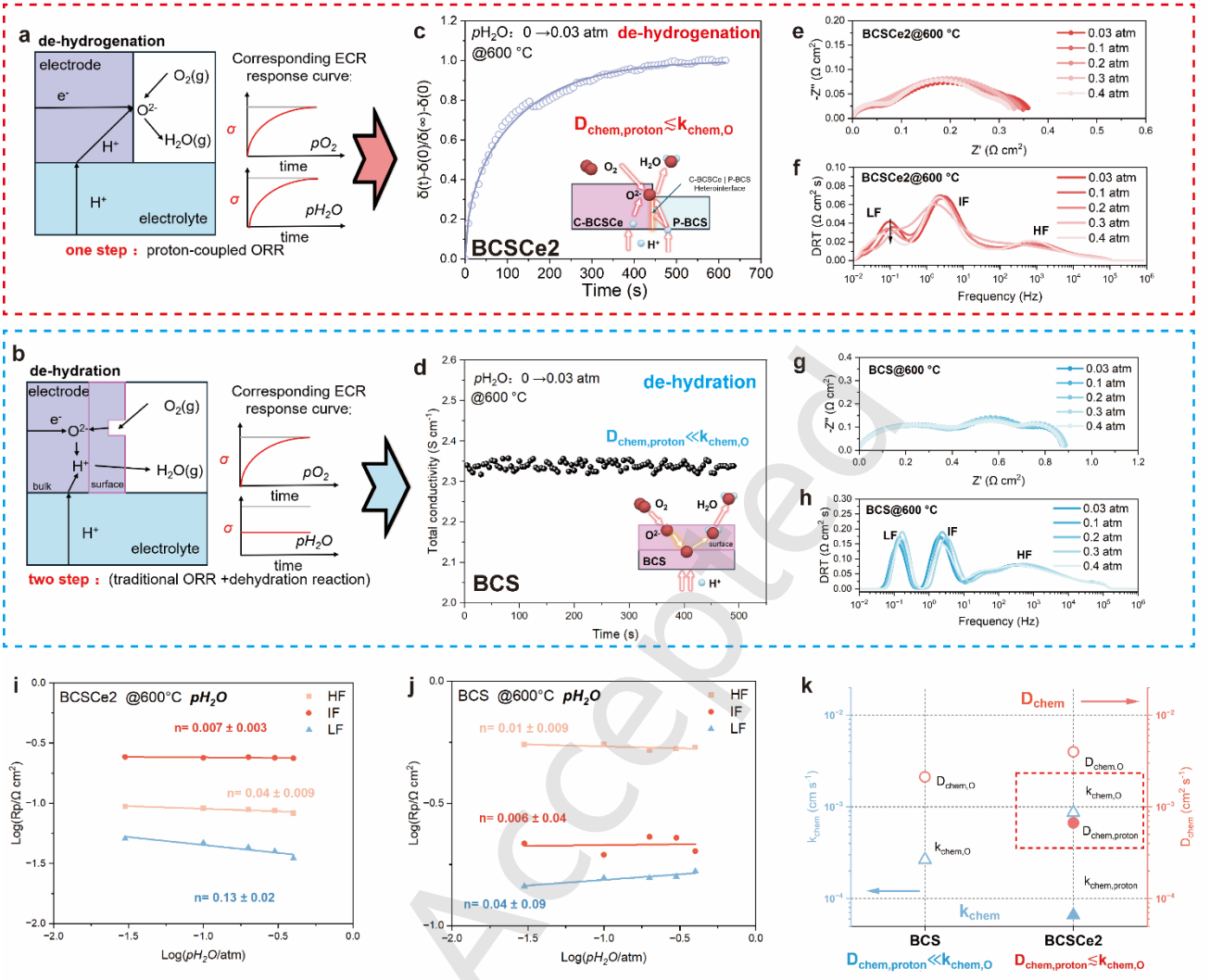


Figure 4. The mechanism diagrams of (a) de-hydrogenation and (b) de-hydration of PC-ORR mechanism . ECR curves of (c) BCSCe2 and (d) BCS samples. The (e) EIS plots and (f) DRT curves of BCSCe2 under different vapor partial pressure. The (g) EIS plots and (h) DRT curves of BCSCe2 under different vapor partial pressure. Dependence of deconvoluted iF (i = H, I, and L) (i) BCSCe2 and (j) BCS as a function of pH_2O. (k) D_{chem} and k_{chem} for BCSCe2 and BCS sample;

3.5 Electrode structure design informed by PC-ORR mechanism

Given the distinct PC-ORR mechanisms governing BCSCe2 and BCS oxygen electrodes, a rational microstructure modification strategy must be tailored accordingly, taking into account their unique sintering behaviors. Hence, the sintering characteristics of the Ce/Sc-doped BCO series powders was systematically investigated. As shown in Figure S17, SEM reveals that elemental doping

Just Accepted

critically influences the sinterability and particle growth of synthesized-BCO perovskites.[13, 54] Pristine BCO exhibits a highly fragmented, ultrafine particle morphology with poor particle coalescence. This limited particle growth arises from the structural instability intrinsic to undoped BCO: polymorphic phase transitions (hexagonal ↔ cubic) during thermal treatment induce significant internal thermal stresses, impeding continuous crystallite growth and yielding irregular, poorly sintered agglomerates.[25, 26] In contrast, Sc doping stabilizes the perovskite cubic phase and alleviates lattice distortion. As evidenced in Figure S18, BCS powders demonstrate markedly enhanced particle growth during sintering, forming dense particle tens of micrometers in size with distinct grain boundaries and well-developed sintering necks. This confirms that Sc doping substantially improves both structural stability and high-temperature sintering activity in the system.[26] However, the sluggish oxygen surface exchange kinetics, identified as the RDS for the BCS electrode, remains the principal limitation for its electrocatalytic performance.

Considering the hydrogenation PC-ORR mechanism operative in BCSCe2, achieving maximal performance requires a continuous, uninterrupted proton-conducting phase network.[21, 48] To explore the interplay between PC-ORR pathways and electrode microstructure, BCSCe2 powders with distinct particle size were synthesized. Figure 5a shows that nanosized-BCSCe2 (N-BCSCe2) powder possesses an extremely high specific surface area and a loosely agglomerated morphology. Conversely, the micro-sized M-BCSCe2 powder (Figure 5b) retains large, dense particles similar to BCS. EDS mapping further confirms the dual-phase composition of BCSCe2 in Figure S19-20. After calcined on single cell pellets as oxygen electrode, N-BCSCe2 forms a porous structure with very high specific surface area, whereas M-BCSCe2 reveals a characteristic microstructure where smaller particles coat larger particles, forming an intermediate nanoparticle layer through natural agglomeration. Based on the proton transport mechanism analysis, the optimal electrode microstructure fundamentally depends on the intrinsic RDS, rather than a universal maximization of surface area.[21, 48]

Just Accepted

For BCS, which follows a hydration-dehydration PC-ORR mechanism, the RDS is the surface oxygen vacancy-assisted O_2 dissociation—a surface-reaction-inherently benefiting from increased active site exposure via larger surface area.[46] However, Ce doping and formation of P-BCO secondary phase switches the proton uptake of BCSCe2 electrode to a hydrogenation-dehydrogenation mechanism and concomitantly shifts the RDS to bulk proton transport limitation. In this bulk-transport-limited scenario, high surface area nanostructures no longer confer performance advantages.[21, 32, 48] By contrast, large, well-sintered micron-sized particles fabricated via solid-state reaction (SSR) provide continuous, low-defect pathways favorable for proton diffusion, directly targeting the rate-limiting bulk transport process (Figure 5c).[48] Accordingly, the N-BCSCe2 oxygen electrode's electrochemical performance is intrinsically limited by sluggish proton transference in its nanostructured framework.

To investigate the influence of morphology and particle size on the proton uptake capability of BCSCe2 electrode, Time-of-Flight secondary ion mass spectrometry (TOF-SIMS) measurements were performed on M-BCSCe2 and N-BCSCe2 tablets after hydration treatment in 3%H_2O at 600 °C for 24 hours.[25, 53] For BCSCe2 electrodes that follow the hydrogenation mechanism, the initial adsorption of H_2O involves reaction with lattice oxygen and holes, leading to O_2 release and formation of OH^- groups.[28] As shown in Figure 5d, TOF-SIMS spectra reveal distinct OH^- signals ($m/z \approx 17$) in both M-BCSCe2 and N-BCSCe2 samples, confirming proton incorporation within the crystal lattice. [25, 53] Notably, the M-BCSCe2 sample (red curve) exhibits a significantly stronger OH^- signal compared to the N-BCSCe2 sample (blue curve), indicating enhanced proton uptake capacity associated with its larger particle morphology.

Furthermore, bulk proton diffusion properties were investigated via depth profiling (Figure 5e) and 3D mapping (Figure 5f) of the OH^- signal. For depth profiling comparisons, the OH- signals were normalized to the OH^-/O^- ratio. Throughout the entire profiling process, the M-BCSCe2 sample consistently exhibited higher signal intensities than the N-BCSCe2 sample.[25, 53] The higher OH^-/O^-

Just Accepted

concentration along the depth profile in M-BCSCe2 suggests a greater abundance of continuous proton diffusion sites. [25, 53] The complementary 3D OH^- distribution maps (Figure 5f) visually corroborate these observations, showing a more uniform and extensive OH^- coverage on the surface of M-BCSCe2 electrodes compared to N-BCSCe2. This spatial continuity of OH^- in both surface and bulk regions of M-BCSCe2 electrodes likely facilitates efficient proton transport, thereby contributing to the superior electrochemical performance. [25, 53]

To further validate the enhanced proton conduction in M-BCSCe2 sample, the proton conductivity measurements were conducted using an optimized Hebb-Wagner method with BZCYYb serving as blocking electrodes at 200-500 °C under H_2 conduction.[10] This setuo ensures that protons are the sole charge carriers in the BZCYYb|BCSCe2|BZCYYb pellet configuration. In Figure S21a, the structural schematic of BZCYYb|BCSCe2|BZCYYb and compares the proton conductivities of M-BCSCe2 and N-BCSCe2. The dense BZCYYb layers combined with an extremely low pO_2 (~10^{-25} atm)guarantee exclusive proton conduction.[10] Minor cracks observed in BZCYYb layers likely resulted from sample preparation for SEM analysis. As confirmed by EDS mapping (Figure S21b), no secondary reactions occurred between BZCYYb and BCSCe2 powders. Figure S22 illustrate the time dependence of voltage drop under steady-state conditions, where the voltage signals reached saturation within ~100 s, indicating stable proton transfer between the two BZCYYb blocking electrodes, with electrons and oxygen ions fully blocked. The calculated proton conductivities for N-BCSC2 and M-BCSCe2 samples are summarized in Figure S23. From 200 °C to 450 °C, M-BCSCe2 exhibits proton conductivities of 2.11×10^{-6}, 2.15×10^{-5}, 2.96×10^{-5}, 3.32×10^{-4}, 7.76×10^{-4}, and 1.60×10^{-3} S cm^{-1}, respectively, whereas N-BCSCe2 sample shows corresponding values of 2.44×10^{-7}, 5.00×10^{-6}, 3.06×10^{-6}, 1.03×10^{-5}, 4.97×10^{-4}, and 5.25×10^{-4} S cm^{-1}. The activation energy (E_a) calculated for M-BCSCe2 and N-BCSCe2 are 0.836±0.069 eV and 1.048±0.161 eV, respectively, consistent with typical proton conduction values.[10] The lower E_a and the order-of-magnitude higher proton conductivity in M-BCSCe2 highlight the superior proton transport efficiency afforded by larger

Just Accepted

particle powders. Therefore, micron-sized, well-sintered grains in M-BCSCe2 significantly enhance bulk proton conduction.

Electrochemical evaluation (Figure 5 g-i) further confirms the superiority of this microstructure optimized for the proton conduction mechanism. The M-BCSCe2 electrode powders can be synthesized via solid-state reaction method (1000 °C for 5h) or prolonged calcination in sol-gel method (1000 °C for 10h). As shown in Figure S24 and Figure S25, the M-BCSCe2 oxygen electrodes exhibit superior electrochemical performance in symmetrical cells, achieving a low ASR value (0.138 Ω cm^2) at 600 °C. Furthermore, M-BCSCe2 oxygen electrodes (Figure 5h, Figure S24 and S25) deliver higher peak power density (2.28 W cm^{-2}) and electrolysis current density (2.96 A cm^{-2}) at 700 °C compared with the N-BCSCe2 electrode (1.73 W cm^{-2} and 2.81 A cm^{-2}, respectively; Figure 5g, Figure S26 and S27). Additionally, Figure 5 h and S24-25 demonstrate that regardless of synthesis method (sol-gel or solid-state), BCSCe2 electrodes composed of identical elements but larger particle sizes consistently show superior electrochemical performance (ASR of 0.138 — 0.145 Ω cm^2 and power density of 2.28—2.24 W cm^{-2}) versus nanosized counterparts (ASR ~0.37 Ω cm^2 and power density ~1.73 W cm^{-2}). This underscores the dominant role of bulk proton conduction in performance enhancement. Benchmarking in Figure 5i, 5j, and Table S4 reveals that M-BCSCe2 outperforms many recently reported state-of-the-art protonic ceramic fuel cell oxygen electrodes at intermediate temperatures, achieving competitive power densities in the 600–700 °C range.[55-59] Furthermore, comparisons of morphology, specific surface area, porosity, and electrode/electrolyte thickness are provided in Figure S28-30 and Table S5. As shown in Figure S29, N-BCSCe2 sample exhibits a specific surface area of 10.7067 m^2/g, whereas M-BCSCe2 has a significantly lower surface area of 1.176 m^2/g. Porosity measurements, averaged from triplicates, indicate that the M-BCSCe2 possesses higher porosity (24.22 %) compared to N-BCSCe2 (16.93%). SEM images (Figure S30 a) reveal that M-BCSCe2 pellets comprise larger particles with relatively wider interparticle voids, forming a continuous framework beneficial for phase-wise proton conduction. In contrast, the lower porosity of the N-

Just Accepted

BCSCe2 originates from the high sintering activity of its nanosized particles, which may partially obstruct proton transport pathways and consequently limit electrochemical performance.

These findings challenge the conventional assumption that higher surface area invariably yields better electrochemical performance. Instead, they demonstrate that electrode morphology must be designed in concert with the material's intrinsic RDS to maximize catalytic activity. For bulk-transport-limited hydrogenation-type oxygen electrodes, large-particle microstructures enabling continuous proton conduction are a more effective strategy than nanoscale high-Architectures. This mechanism-guided microstructure design paradigm provides a new route for the rational development of high-performance PCCs oxygen electrodes.

Just Accepted

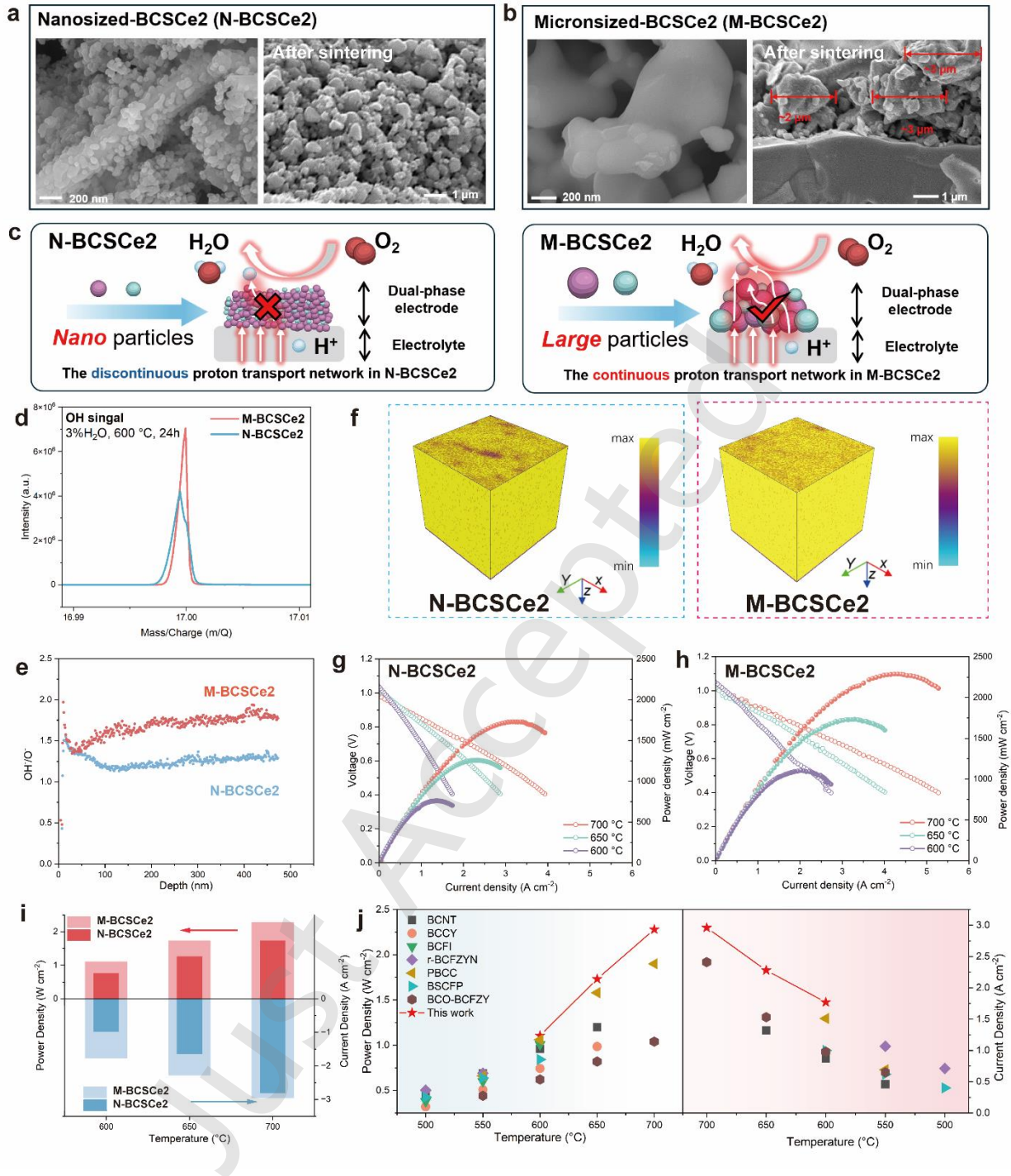


Figure 5. SEM images of (a) N-BCSCe2, and (b) M-BCSCe2 powders. (c) The mechanism diagrams of nanosized N-BCSCe2 and M-BCSCe2 electrode in single cell. (d) TOF-SIMS spectrum, (e) depth profiles (The normalized curves of OH-/O- signal) and (f) 3D maps of OH- signal for M-BCSCe2 and N-BCSCe2 samples after H_2O exchange treatment at 600 °C. The I-V-P plots of (g) N-BCSCe2 and (h) M-BCSCe2 electrode in fuel cell mode. (i) The comparison of power density and electrolysis current density between M-BCSCe2 and N-BCSCe2. (j) The comparison of power density and electrolysis current density among recently reported oxygen electrodes.

Just Accepted

4 Conclusions

In summary, this work addresses the sintering instability and sluggish oxygen electrode kinetics inherent to conventional $BaCoO_3$-based materials by developing a Sc-Ce dual-doping induced in-situ particle gradation strategy, grounded on the differentiation of proton-coupled oxygen reduction reaction (PC-ORR) mechanisms. Sc doping effectively stabilizes the cubic perovskite lattice, mitigating sintering-induced microcracks and enhancing structural integrity. Beyond solubility limits, Ce doping triggers in-situ phase reconstruction, resulting in a dual-phase architecture composed of a coarse C-BCSCe catalytic framework interspersed with nano-sized proton-conducting P-BCO fillers. This composite design simultaneously reduces thermal expansion mismatch, strengthens interfacial bonding, and establishes continuous proton conduction pathways. Most critically, this work systematically elucidates the PC-ORR pathways in the $BaCoO_3$-based oxygen electrode system, revealing a fundamental mechanistic transition. The pristine BCS electrode follows a hydration-dehydration mechanism, wherein the RDS is surface oxygen vacancy-mediated O_2 dissociation. In contrast, the BCSCe2 electrode operates via a hydrogenation-dehydrogenation PC-ORR pathway, with proton migration identified as the potential RDS. This mechanistic distinction reveals that high surface area is not always the dominant factor for catalytic enhancement in dual-phase electrodes.

Guided by the identified RDS, the BCSCe2 oxygen electrode was rationally engineered with a large- particle microstructure fabricated via the solid-state reaction. Compared to nanoscale, high-surface-area morphologies, micron-sized, well-sintered particles maintain continuous bulk conduction channels, effectively addressing the bulk-transport-limited reaction regime. Coupled with a regulated electronic structure—characterized by enriched high-spin Co^{3+} species, abundant oxygen vacancies, and weakened Co-O bonds—this optimized oxygen electrode simultaneously achieves enhanced ORR/OER electrocatalytic activity and long-term operational durability. Electrochemical measurements validate that the BCSCe2 electrode attains a low polarization resistance of 0.138 $\Omega \cdot cm^2$ at 600 °C and maintains stable operation over 120 hours. Single cell tests demonstrate a peak power

Just Accepted

density of 2.28 $W \cdot cm^{-2}$ and an electrolysis current density of 2.96 $A \cdot cm^{-2}$ at 700 °C, outperforming most reported Co-based PCC oxygen electrodes. Beyond demonstrating a facile and scalable synthesis route for advanced dual-phase oxygen electrodes, this work establishes a robust mechanism-guided design paradigm integrating reaction pathway identification, RDS analysis, and microstructure matching. Such an approach offers a valuable framework for the rational development of next-generation protonic ceramic electrochemical devices.

Acknowledgements

This work was supported by the National Natural Science Foundation of China (Nos. 51502136), the Natural Science Foundation of Jiangsu Province (No. BK 20211260), Postgraduate Research & Practice Innovation Program of Jiangsu Province (26CXJH2720), the Priority Academic Program Development (PAPD) of Jiangsu Higher Education Institutions, and the Top-notch Academic Programs Project of Jiangsu Higher Education Institutions (TAPP)..

Funding

the National Natural Science Foundation of China (Nos. 51502136),

the Natural Science Foundation of Jiangsu Province (No. BK 20211260),

Postgraduate Research & Practice Innovation Program of Jiangsu Province (26CXJH2720),

the Priority Academic Program Development (PAPD) of Jiangsu Higher Education Institutions,

the Top-notch Academic Programs Project of Jiangsu Higher Education Institutions (TAPP).

Author contributions

Lin Ge : Conceptualization, Funding acquisition, Supervision, Writing-review and editing.

Just Accepted

Xiaole Yu :Conceptualization, Methodology, Validation, Visualization, Formal analysis, Investigation, Writing-original draft.

Xinyuan Zhao : Investigation, Validation, Formal analysis, Writing-original draft.

Bingyu He : Validation, Visualization, Formal analysis.

Maoyi Hua : Validation, Visualization, Formal analysis.

Yue Luo : Validation, Visualization, Formal analysis.

Ziru Li : Validation, Visualization, Formal analysis.

Jida Wang : Validation, Visualization, Formal analysis.

Sheng Cui : Funding acquisition, Supervision, Writing-review and editing.

Availability of data and materials

The data that support the findings of this study are available from the corresponding author upon reasonable request.

Competing interests

The authors have no competing interests to declare that are relevant to the content of this article.

Electronic Supplementary Material

Supplementary material is available in the online version of this article

References

[1] Bian WJ, Wu W, Wang BM, et al. Revitalizing interface in protonic ceramic cells by acid etch. Nature, 2022, **604**: 479-485.

[2] Duan CC, Kee Robert J, Zhu HY, et al. Highly durable, coking and sulfur tolerant, fuel-flexible protonic ceramic fuel cells. Nature, 2018, **557**: 217-222.

[3] Dai HL, Boulfrad S, Chu XR, et al. $La_{0.5-x}Sc_xSr_{0.5}MnO_{3-\delta}$ cathodes for proton-conducting solid oxide fuel cells: Taking advantage of the secondary phase. Journal of Advanced Ceramics, 2024, **13**: 1759-1770.

Just Accepted

[4] Dai HL, Du HZ, Boulfrad S, et al. Manipulating Nb-doped $SrFeO_{3-\delta}$ with excellent performance for proton-conducting solid oxide fuel cells. Journal of Advanced Ceramics, 2024, **13**: 579-589.
[5] Dai HL, Du HZ, Liu Z, et al. Multi-element doped $SrFeO_3$-based cathodes with balanced thermal expansion for proton-conducting solid oxide fuel cells. Journal of Advanced Ceramics, 2025, **14**: 9221165.
[6] Li ZH, Mao X, Feng DS, et al. Prediction of perovskite oxygen vacancies for oxygen electrocatalysis at different temperatures. Nature Communications, 2024, **15**: 9318.
[7] Zhang XX, He HY, Chen Y, et al. Co-expression of multi-genes for polynary perovskite electrocatalysts for reversible solid oxide cells. Nature Communications, 2025, **16**: 2868.
[8] Li M, Liu F, Ding D Critical insights into the steam electrolysis electrode in protonic ceramic cells for hydrogen production. Nature Catalysis, 2025, **8**: 293–300.
[9] Liu F, Deng H, Diercks D, et al. Lowering the operating temperature of protonic ceramic electrochemical cells to< 450° C. Nature Energy, 2023, **8**: 1145-1157.
[10] Yu XL, Ge L, Wu BZ, et al. Ultra durable composite steam electrode with cube-shaped $BaZr_{0.85}Y_{0.15}O_{3-\delta}$ facet-boosted efficiency toward advanced protonic ceramic electrolysis cells. Journal of Advanced Ceramics, 2025, **14**: 9221036.
[11] Zhang SY, Dou YN, Xia T, et al. Achieving electrocatalytic activity toward oxygen reduction reaction based on Ruddlesden–Popper type cathode catalyst for solid oxide fuel cells. Journal of Advanced Ceramics, 2025,
[12] Wu SY, Yan WY, Ni N, et al. Densification of ceria-based barrier layer for solid oxide cells at lower sintering temperatures: A review. Journal of Advanced Ceramics, 2025, **14**: 9221001.
[13] Tang W, Bian WJ, Ding HP, et al. Sintering protonic zirconate cells with enhanced electrolysis stability and Faradaic efficiency. Nature Synthesis, 2025, **4**: 592-602.
[14] Liu YY, Luo J, Li C, et al. $BaCe_{0.8}Fe_{0.1}Ni_{0.1}O_{3-\delta}$-impregnated Ni–GDC by phase-inversion as an anode of solid oxide fuel cells with on-cell dry methane reforming. Journal of Advanced Ceramics, 2024, **13**: 834-841.
[15] Wan BF, Liu T, Chang YL, et al. Thermodynamic NiO exsolution for durable and efficient cobalt-free cathodes in proton-conducting solid oxide fuel cells. Journal of Advanced Ceramics, 2025,
[16] Cao JF, Ji YX, Shao ZP. Perovskites for protonic ceramic fuel cells: a review. Energy Environmental Science, 2022, **15**: 2200-2232.
[17] Li T, Yang YJ, Yang F, et al. High-oxygen vacancy cerium catalysts with NiFe alloy heterostructures: A pathway for efficient and stable biomass ethanol fuel tubular solid oxide fuel cells. Journal of Advanced Ceramics, 2025, **14**: 9221143.
[18] Gu YH, Chen ZY, Wang ZC, et al. Avoiding undesirable cathode/electrolyte interfacial reactions for proton-conducting solid oxide fuel cells by Joule heating. Journal of Advanced Ceramics, 2025, **14**: 9221040.
[19] Zhou L, Yin YR, Nematov D, et al. A high-performance cobalt-free cathode for proton-conducting solid oxide fuel cells via multi-element doping in $Sr_2Fe_2O_6$. Sustainable Materials and Technologies, 2026, **48**: e01936.
[20] Tian HC, Li W, Lee Y-L, et al. Conformally coated scaffold design using water-tolerant $Pr_{1.8}Ba_{0.2}NiO_{4.1}$ for protonic ceramic electrochemical cells with 5,000-h electrolysis stability. Nature Energy, 2025, **10**: 890–903.
[21] Geng YQ, Zheng SL, Karki S, et al. Nano-Engineered Interfaces in Dual-Layer Electrodes for Protonic Ceramic Cells with Enhanced Stability and Kinetics. ACS nano, 2025, **19**: 42566-42579.
[22] Zhou L, Liu YP, Li C, et al. Application of $Sr_2Fe_{2-x}Mo_xO_{6-\delta}$-Based Double Perovskite Materials in Solid Oxide Cells. Advanced Ceramics, 2025, **46**: 485-519.
[23] Dai HL, Bi L. High-Entropy Cathodes for Proton-Conducting Solid Oxide Fuel Cells: A Promising Yet Uncharted Frontier. 2026, **6**: e70054.
[24] Song WH, Dong XC, Yin YR, et al. Reviving the activity of Si-contaminated cathodes via chloride anion doping for proton-conducting solid oxide fuel cells. Journal of Advanced Ceramics, 2026, **15**: 9221262.
[25] Zhang WW, Wang S, Yang CH, et al. Dual-Donor Doped Perovskite as Bifunctional Oxygen Electrode Catalyst for Reversible Protonic Ceramic Electrochemical Cell. Journal of the American Chemical Society, 2025, **147**: 43584-43593.
[26] Kim DY, Jeong I, Ahn SJ, et al. On the Role of Bimetal-Doped $BaCoO_3$ Perovskites as Highly Active Oxygen Electrodes of Protonic Ceramic Electrochemical Cells. Advanced Energy Materials, 2024, **14**: 2304059.
[27] Chen X, Tan YS, Li Z, et al. Advanced air electrodes for reversible protonic ceramic electrochemical cells: A comprehensive review. Advanced Materials, 2025: 2418620.
[28] Kim SC, Yoon DG, Chae JW, et al. Elucidating the proton-coupled oxygen reduction pathway in protonic ceramic fuel cells. Energy Environmental Science 2026, **19**: 1715-1731.
[29] Yu XL, Zhao ZN, He BY, et al. Time-phase-controlled exsolution of FeCoNi ternary alloy nanoparticles on perovskite anode catalyst for enhanced dual-functional catalysis and protection in ammonia-fueled protonic ceramic fuel cells. Journal of Materials Chemistry A, 2026,
[30] Ge L, Yu XL, Zhao ZN, et al. Defect-engineered heterogeneous interfaces for enhanced activity and durability in protonic ceramic cell air electrodes. Transactions of Materials Research, 2025: 100141.
[31] Liu ZQ, Bai YS, Sun HN, et al. Synergistic dual-phase air electrode enables high and durable performance of reversible proton ceramic electrochemical cells. Nature communications, 2024, **15**: 472.

Just Accepted

[32] Zheng SL, Kumari A, Geng YQ, et al. Interfacial Nanostructuring Enables Integrated, Low‐Polarization Reversible Protonic Ceramic Cells. Advanced Energy Materials, 2026, **16**: e70850.
[33] Yin YR, Yu SF, Gu YY, et al. Turning the bilayer upside down delivers a record-high Ba/Co-free cathode for proton-conducting solid oxide fuel cells. Energy & Environmental Science, 2026,
[34] Zhang Y, Wang YB, Liu ZL, et al. Constructing Robust and Efficient Ceramic Cells Air Electrodes Through Collaborative Optimization Bulk and Surface Phases. Advanced Functional Materials, 2025: 2422531.
[35] He BY, Yu XL, Yu ZX, et al. Controllable Jahn‐Teller Distortion Engineering Enables in‐situ Self‐assembly Phase‐Reconstruction for High‐Performance Protonic Ceramic Cell Air Electrodes. Advanced Functional Materials, 2026: e76725.
[36] Yang HX, Zhang Y, Liu ZP, et al. Hydration-induced stiffness enabling robust thermal cycling of high temperature fuel cells cathode. Nature communications, 2025, **16**: 3154.
[37] Zhang Y, Chen B, Guan DQ, et al. Thermal-expansion offset for high-performance fuel cell cathodes. Nature, 2021, **591**: 246-251.
[38] Poetzsch D, Merkle R, Maier J Oxygen reduction at dense thin-film microelectrodes on a proton-conducting electrolyte: I. Considerations on reaction mechanism and electronic leakage effects. Journal of The Electrochemical Society, 2015, **162**: F939-F950.
[39] Wang DH, Li T, Wang YK, et al. Cerium‐entropy coupling boosts oxygen vacancy density and bifunctional oxygen electrocatalysis in reversible protonic ceramic electrochemical cells. Advanced Functional Materials, 2026, **36**: e25122.
[40] Clark S J, Segall M D, Pickard C J, et al. First principles methods using CASTEP. Zeitschrift für kristallographie-crystalline materials, 2005, **220**: 567-570.
[41] Xu Yangsen, Gu Yueyuan, Bi Lei. A highly-active $Zn_{0.58}Co_{2.42}O_4$ spinel oxide as a promising cathode for proton-conducting solid oxide fuel cells. Journal of Materials Chemistry A, 2022, **10**: 25437-25445.
[42] Zhang M, Liu JY, Du ZH, et al. Highly active and stable oxygen electrode $PrBaCo_2O_{5+\delta}$-Ba_2CoWO_6 enabled by In Situ formed misfit dislocation interface for reversible solid oxide cell. Applied Catalysis B: Environment & Energy 2025, **361**: 124669.
[43] Yu XL, Ge L, Mi YW, et al. Superior Active and Durable Air Electrode for Protonic Ceramic Cells by Metal‐Oxide Bond Engineering. Small, 2025: 2408607.
[44] Yin YR, Zhang SQ, Wang A, et al. Rational design of $PrBaFe_2O_{6-\delta}$-based cathodes for protonic ceramic fuel cells. Journal of Advanced Ceramics, 2024, **13**: 1600-1610.
[45] Zhu K, Zhang LJ, Shi N, et al. A superior catalytic air electrode with temperature-induced exsolution toward protonic ceramic cells. ACS nano, 2024, **18**: 5141-5151.
[46] Zheng SL, Geng YQ, Islam S, et al. Vacancy‐Redox Coupling at Interface‐Engineered Heterostructures Enhances Reversible Energy Conversion in Protonic Ceramic Cells. Angewandte Chemie International Edition, 2026, **65**: e7079252.
[47] Liu CZ, Liu B, Li ZF, et al. Interface-engineering to boost the performance and durability of nickel-metal-supported reversible proton ceramic cells for power generation and hydrogen production. Journal of Advanced Ceramics, 2025, **14**: 9221115.
[48] Kim D, Lee DG, Kim HW, et al. Quantitative Interface Engineering Framework for High‐Performance and Durable Protonic Ceramic Electrochemical Cells. Advanced Energy Materials 2026, **16**: e70809.
[49] Song YX, Song YF, Wang YH, et al. Cation‐Selective Defects Engineering in A‐Site Ordered Layered Perovskites for High‐Performance Reversible Protonic Ceramic Cells. Advanced Materials, 2025, **37**: e11519.
[50] Duan YC, Li H, Li SQ, et al. Thermal Expansion Matching as a Key Criterion for Developing High‐Performance Mn‐based Mullite Cathodes in SOFCs. Advanced Materials, 2026: e13615.
[51] He F, Hou MY, Liu DL, et al. Phase segregation of a composite air electrode unlocks the high performance of reversible protonic ceramic electrochemical cells. Energy Environmental Science, 2024, **17**: 3898-3907.
[52] Shi N, Xie Y, Hu XY, et al. A Highly Hydrophilic Air Electrode With Water‐Induced Surface Reconstruction for Efficient Reversible Protonic Ceramic Cell at Low Water Partial Pressures. Advanced Energy Materials, 2026: e71076.
[53] Zhai S, Hao SR, Zhao RB, et al. A constricted potassium evaporation strategy promoting ordered segregation for superior air electrodes in protonic ceramic fuel cells. Joule, 2026: 102435.
[54] Gong JY, Du KP, Jiang W, et al. Controlled growth of $Pr_{1.5}Ba_{1.5}Cu_3O_7$ cubes to meliorate the cathode reaction for protonic ceramic fuel cells. Journal of Advanced Ceramics, 2025, **14**: 9221060.
[55] Zhou YC, Liu EZ, Chen Y, et al. An Active and Robust Air Electrode for Reversible Protonic Ceramic Electrochemical Cells. ACS Energy Letters, 2021, **6**: 1511-1520.
[56] Wu J, Xie ZH, Liang MZ, et al. A new nanocomposite electrode developed from environmental atmosphere triggered reconstruction for efficient reversible protonic ceramic cells. Advanced Energy Materials, 2025, **15**: 2404118.

Just Accepted

[57] Liu ZQ, Cheng DF, Zhu YL, et al. Robust bifunctional phosphorus-doped perovskite oxygen electrode for reversible proton ceramic electrochemical cells. Chemical Engineering Journal, 2022, **450**: 137787.

[58] Song YF, Chen YB, Wang W, et al. Self-assembled triple-conducting nanocomposite as a superior protonic ceramic fuel cell cathode. Joule, 2019, **3**: 2842-2853.

[59] Zhang XY, Wang CX, Liu K, et al. Significantly enhanced stability and activity of a perovskite oxygen electrode for reversible protonic ceramic electrochemical cells by heterointerface engineering. Journal of Advanced Ceramics, 2025, **14**: 9221108.

Just Accepted